Int. J. Heat Mass Transfer. Vol. 32, No. 6, pp. 1007–1019, 1989
Printed in Great Britain

0017–9310/89 $3.00+0.00

The transient behavior of weldpools with a deformed free surface

M. E. THOMPSON† and J. SZEKELY
Department of Materials Science and Engineering, Massachusetts Institute of Technology, Cambridge, MA 02139, U.S.A.

(*Received* 18 *September* 1988 *and in final form* 27 *June* 1988)

Abstract—Transient heat transfer, fluid flow and phase change in a weldpool with a deformed free surface are modelled using a two-dimensional coordinate transformation. The theoretical approach makes it possible to accurately model high Marangoni number flows even when the free surface is not horizontal. The method is used to examine the role of surface deformation and surface tension forces in controlling weld penetration during cathode spot welding of steel and aluminum. The calculated flow fields, temperature distributions and weldpool shapes are consistent with experimental findings, and are in reasonable agreement with previously published modelling efforts.

INTRODUCTION

IN RECENT years, there has been an increased effort to develop mathematical models to describe the phenomena occurring during GTA welding, laser welding and electron beam welding, the ultimate goal of these investigations being to determine how the process parameters affect weldment quality.

Most welding operations have the common feature that a heat source is applied to the top surface of a metal block, which heats up, eventually forming a liquid pool. The subsequent solidification of this pool causes the desired joining process. Among the major practical issues are the rate of heat transfer and the time-dependent shape of the weldpool during both its growth and its collapse. The weldpool geometry and the transient evolution of the temperature profiles will play a major role in determining the solid structure.

The earlier models of welding processes, which involved conductive heat transfer only, are now being superseded by more appropriate models in which allowance is made for convective effects, as driven by the combination of surface tension, buoyancy, and electromagnetic forces.

However, even these models have involved a degree of idealization, in postulating quasi-steady conditions, predetermined weldpool shapes and, with few exceptions, a flat weldpool top surface.

It is an established fact that in many welding applications, significant free surface deformation will occur, at times producing craters of comparable dimension to the weldpool itself. The effect of these depressions has yet to be fully explored.

The purpose of this work is to develop a mathematical model which accurately predicts heat transfer and fluid flow phenomena in weldpools with depressed free surfaces.

MATHEMATICAL FORMULATION OF THE PROBLEM

Figure 1 is a schematic diagram of the idealized weldpool and workpiece to be considered. The plasma arc or laser supplies thermal energy to the surface of the workpiece, producing a molten region. The incoming heat flux is assumed to be Gaussian in form [1, 2], and is balanced by vaporization and radiative and convective losses at the free surface, as well as by convection within the molten pool. The temperature gradient along the free surface induces Marangoni convection, while thermal gradients within the pool result in buoyancy-driven motion. In addition, the balance between convective and conductive heat transfer in the pool and the surrounding solid controls the rate at which the molten region expands or contracts through the workpiece.

The following assumptions have been made.

(1) The weldpool is represented as a two-dimensional slice.

(2) The fluid motion is laminar and controlled by buoyancy and surface tension forces (electromagnetic effects excluded).

(3) The Boussinesq approximation is used.

(4) The surface tension is a function of temperature with the surface tension coefficient assumed to be a constant.

(5) The workpiece is stationary relative to the heat source.

(6) Radiation and vaporization effects are excluded from the energy balance at the free surface.

(7) The temperature at the free surface is not allowed to exceed the vaporization temperature.

Although electromagnetic forces have been neglected, this is not likely to produce serious errors, as under many conditions the velocity field will be governed primarily by the surface tension forces [3–5].

Since the convective motion in the pool will be

† Present address: Division 6233, Sandia National Laboratories, Sandia, NM 87185, U.S.A.

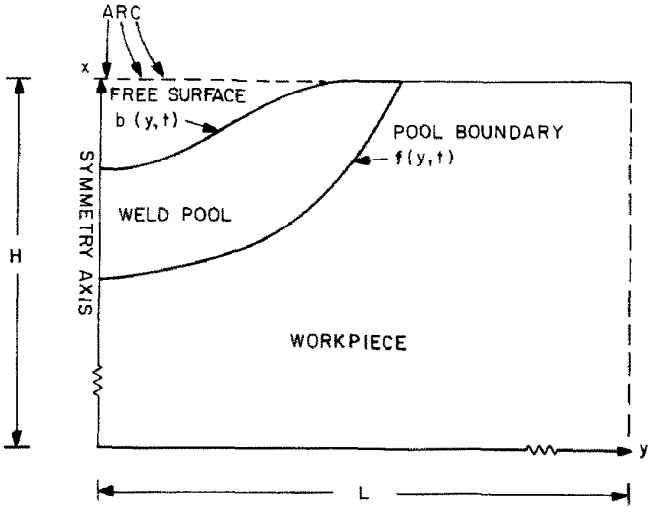

FIG. 1. Schematic diagram of the weldpool and coordinate system.

coupled to the free surface and internal heat transfer processes, the transient velocity and thermal fields must be calculated simultaneously. The dimensionless form of the momentum equations are written in Cartesian coordinates in terms of the stream function (ψ) and vorticity (ω) as (variables defined in Table 1, dimensionless parameters in Table 3

$$\frac{\partial\omega'}{\partial t}+A^2u'\frac{\partial\omega'}{\partial x'}+Av'\frac{\partial\omega'}{\partial y'}-Ra\,Pr\,A\frac{\partial\theta}{\partial y'}$$

$$=Pr\left(\frac{\partial^2\omega'}{\partial x'^2}+A^2\frac{\partial^2\omega'}{\partial y'^2}\right) \quad (1)$$

$$-\omega'=\left(\frac{\partial^2\Psi'}{\partial x'^2}+A^2\frac{\partial^2\Psi'}{\partial y'^2}\right). \quad (2)$$

The thermal energy within the molten region is described by

$$\frac{\partial\theta}{\partial t'}+A^2u'\frac{\partial\theta}{\partial x'}+Av'\frac{\partial\theta}{\partial y'}=\left(\frac{\partial^2\theta}{\partial x'^2}+A^2\frac{\partial^2\theta}{\partial y'^2}\right) \quad (3)$$

while that within the solid workpiece is given by

$$\frac{\partial\theta}{\partial t'}=\alpha\left(\frac{\partial^2\theta}{\partial x'^2}+A^2\frac{\partial^2\theta}{\partial y'^2}\right). \quad (4)$$

The boundary conditions for the momentum equations express the 'no-slip' condition at the solid surfaces

$$V\cdot n_f=V\cdot t_f=0$$

where V is the velocity vector and n_f, t_f are the unit vectors normal and tangential to the phase boundary. Along the solid boundary ($x=f(y,t)$) and at the free surface ($x=b(y,t)$), the stream function is a constant

$$\Psi'=0.$$

In addition, at the axis of symmetry ($y=0$)

$$v'=0$$

Table 1. Table of symbols (primes denote dimensionless quantities, and asterisks denote transformed variable)

$x'=\frac{x}{H}$	vertical coordinate
$y'=\frac{y}{L}$	horizontal coordinate
$F(y,t)=\frac{f(y,t)}{H}$	phase boundary
$B(y,t)=\frac{b(y,t)}{H}$	free surface
$x^*=\frac{x'-F(y,t)}{B(y,t)-F(y,t)}$	transformed vertical coordinates
$y^*=y'$	transformed horizontal coordinate
$t^*=t'=\frac{\kappa t}{H^2}$	time
$v'=\frac{vH}{\kappa}$	horizontal velocity
$u'=\frac{uL^2}{\kappa H}$	vertical velocity
$\omega'=\frac{\omega H^3}{\kappa L}$	vorticity
$\Psi'=\frac{\Psi H}{\kappa L}$	stream function
$\theta=\left(\frac{T_l-T_a}{T_m-T_a}\right)$	temperature in liquid
$\Theta=\left(\frac{T_s-T_a}{T_m-T_a}\right)$	temperature in solid
L	scale for length
H	scale for height
$\Delta T=1420$	reference temperature drop
$T_m=1723$	liquidus temperature
$T_a=298$	ambient temperature
ΔT_s	superheat

and

$$\frac{\partial u'}{\partial y'} = 0.$$

Finally, at the free surface, the relationship between the shear stress and the temperature gradient is expressed as

$$\left(\frac{\partial v}{\partial x} n_b\right) = -\frac{1}{\mu}\frac{\partial \gamma}{\partial T}(t_b \cdot \nabla\theta)$$

where n_b and t_b are the unit vectors normal and tangential to the free surface, and $\partial\gamma/\partial T$ is the surface tension coefficient.

The thermal boundary condition at the free surface is

$$-k_l(n_b \cdot \nabla\theta) = \frac{q(y)L}{\Delta T}.$$

The function $q(y)$ represents the (Gaussian) heat flux from the source of the form

$$q(y) = \frac{3Q}{\pi a^2}\left[\exp\left(-\frac{3y^2}{a^2}\right)\right] = A[\exp(-By^2)]$$

where Q is the power input in W, A in W m^{-2} and a is the effective radius of the power distribution. At the axis of symmetry

$$\frac{\partial\theta}{\partial y'} = \frac{\partial\Theta}{\partial y'} = 0.$$

The temperature at the phase boundary is assumed to be a constant equal to the melt temperature of the material

$$\theta = \Theta = 1.0.$$

Furthermore, the base and the outermost boundaries are assumed to be at ambient temperature

$$\theta = \Theta = 0.$$

In addition, at the solid–liquid interface, the temperature gradients in the solid and liquid phases must satisfy the Stefan condition

$$(n_f \cdot \nabla\theta) - K(n_f \cdot \nabla\Theta) = St\, V_n$$

where V_n, the normal velocity of the phase boundary $[f(y, t)]$, is defined in terms of the unit normal to the phase boundary (n_f) as

$$V_n = v \cdot n_f.$$

To represent the irregular boundaries, a coordinate transformation due to Landau [6–14] has been adopted.

The independent variable in transformed space (x^*) is related to the vertical coordinate in physical space (x') according to

$$x^* = \frac{x' - F(y, t)}{[B(y, t) - F(y, t)]} \tag{5}$$

where $F(y, t)$ and $B(y, t)$ are dimensionless functions which define the locations of the solid and free surfaces of the weldpool, respectively. The transformation maps the irregularly-shaped liquid and solid regions into rectangular computational domains in which the two curvilinear surfaces are stationary during any given time interval, and are defined by

$$x^* = 0 \quad \text{and} \quad 1.0.$$

Using equation (5), the conservation equations in the liquid region can be rewritten as follows:

$$\frac{\partial\omega'}{\partial t'} + \frac{\partial\omega'}{\partial x^*}\frac{\partial x^*}{\partial t'} + A^2 u'\frac{\partial\omega'}{\partial x^*}\frac{\partial x^*}{\partial x'} + Av'\frac{\partial\omega'}{\partial y'} + Av'\frac{\partial\omega'}{\partial x^*}\frac{\partial x^*}{\partial y'} = Pr\left[Ra\,A\left(\frac{\partial\theta}{\partial y'} + \frac{\partial x}{\partial y'}\frac{\partial\theta}{\partial x^*}\right) + \left(\frac{\partial x^*}{\partial x'}\right)^2\frac{\partial^2\omega'}{\partial x^{*2}} + A^2\frac{\partial^2\omega'}{\partial y'^2}\right] + Pr\,A^2\left[2\frac{\partial x^*}{\partial y'}\frac{\partial^2\omega'}{\partial x^*\partial y'} + \frac{\partial^2 x^*}{\partial y'^2}\frac{\partial\omega'}{\partial x^*} + \left(\frac{\partial x^*}{\partial y'}\right)^2\frac{\partial^2\omega'}{\partial x^{*2}}\right] \tag{6}$$

for the vorticity, while the stream function is given as

$$-\omega' = \left(\frac{\partial x^*}{\partial x'}\right)^2\frac{\partial^2\Psi'}{\partial x'^2} + A^2\frac{\partial^2\Psi'}{\partial y'^2} + A^2\left[2\frac{\partial x^*}{\partial y'}\frac{\partial^2\Psi'}{\partial x^*\partial y'} + \frac{\partial^2 x^*}{\partial y'^2}\frac{\partial\Psi'}{\partial x^*} + \left(\frac{\partial x^*}{\partial y'}\right)^2\frac{\partial^2\Psi'}{\partial x^{*2}}\right]. \tag{7}$$

The temperature of the liquid in transformed coordinates is given as

$$\frac{\partial\theta'}{\partial t'} + \frac{\partial\theta'}{\partial x^*}\frac{\partial x^*}{\partial t'} + A^2 u'\frac{\partial\theta'}{\partial x^*}\frac{\partial x^*}{\partial x'} + Av'\frac{\partial\theta'}{\partial y'} + Av'\frac{\partial\theta'}{\partial x^*}\frac{\partial x^*}{\partial y'} = \left(\frac{\partial x^*}{\partial x'}\right)^2\frac{\partial^2\theta'}{\partial x^{*2}} + A^2\frac{\partial^2\theta'}{\partial y'^2} + A^2\left[2\frac{\partial x^*}{\partial y'}\frac{\partial^2\theta'}{\partial x^*\partial y'} + \frac{\partial^2 x^*}{\partial y'^2}\frac{\partial\theta'}{\partial x^*} + \left(\frac{\partial x^*}{\partial y'}\right)^2\frac{\partial^2\theta'}{\partial x^{*2}}\right] \tag{8}$$

where the derivatives in the above equations are defined as

$$\frac{\partial x^*}{\partial t'} = -\frac{1}{B-F}\left[\frac{\partial F}{\partial t'} + x^*\left(\frac{\partial B}{\partial t'} - \frac{\partial F}{\partial t'}\right)\right]$$

$$\frac{\partial x^*}{\partial y'} = -\frac{1}{B-F}\left[\frac{\partial F}{\partial y'} + x^*\left(\frac{\partial B}{\partial y'} - \frac{\partial F}{\partial y'}\right)\right]$$

$$\frac{\partial^2 x^*}{\partial y'^2} = \frac{-1}{B-F}\left[\frac{\partial^2 F}{\partial y'^2} + 2\frac{\partial x^*}{\partial y'}\left(\frac{\partial B}{\partial y'} - \frac{\partial F}{\partial y'}\right) + x^*\left(\frac{\partial^2 B}{\partial y'^2} - \frac{\partial^2 F}{\partial y'^2}\right)\right]$$

$$\frac{\partial x^*}{\partial x'} = \left(\frac{1}{B-F}\right).$$

In the solid phase, the transformed energy equation is written as

$$\frac{\partial\Theta}{\partial t'}+\frac{\partial\Theta}{\partial x^*}\frac{\partial x^*}{\partial t'}=\alpha\left[\left(\frac{\partial x^*}{\partial x'}\right)^2\frac{\partial^2\Theta}{\partial x^{*2}}+A^2\frac{\partial^2\Theta}{\partial y'^2}\right]$$
$$+\alpha A^2\left[2\frac{\partial x^*}{\partial y'}\frac{\partial^2\theta}{\partial x^*\partial y'}+\frac{\partial^2 x^*}{\partial y'^2}\frac{\partial\theta}{\partial x^*}+\left(\frac{\partial x^*}{\partial y^2}\right)^2\frac{\partial^2\theta}{\partial x^{*2}}\right]$$

where the transformed coordinate (x^*) in the solid phase is related to the vertical coordinate in the solid (x') according to

$$x_s^*=\frac{x_s'}{F(y,t)}$$

and the corresponding derivatives (subscripts omitted) are defined as follows:

$$\frac{\partial x^*}{\partial t'}=-\frac{x^*}{F}\frac{\partial F}{\partial t'}$$
$$\frac{\partial x^*}{\partial x'}=\frac{1}{F}$$
$$\frac{\mathrm{d}x^*}{\mathrm{d}y'}=-\frac{x^*}{F}\frac{\mathrm{d}F}{\mathrm{d}y'}$$
$$\frac{\partial^2 x^*}{\partial y'^2}=-\frac{x^*\partial^2 F}{F\partial y'}+\frac{2x^*}{F^2}\left(\frac{\partial F}{\partial y'}\right)^2. \quad (9)$$

When the movement of the melt–solid interface is slow relative to the magnitude of the melt velocity, terms involving $\partial F/\partial t$ may be neglected. This condition is generally applicable for Stefan numbers of ~ 1 [7, 9, 10, 13], and therefore applies to the weld penetration stage for most welding applications. If the free surface profile is moderately smooth and the depression is small relative to the horizontal dimension, terms which involve the derivatives $\partial B/\partial y$ and $\partial^2 B/\partial y^2$ may also be neglected. For the purpose of the calculations to be discussed below, the free surface has been assigned an initial position which remains fixed throughout the time interval examined, so that terms involving $\partial B/\partial t$ vanish from the transformed equations.

The system of governing equations and boundary conditions in transformed dimensionless space is written in finite difference form using forward-time and centered-space differencing for the diffusive terms, and upwind differencing for the convective terms. The convective terms are handled using the second upwind differencing method [15], a method which avoids artificial diffusion errors and returns something of the second-order accuracy of centered space derivatives. The parabolic vorticity and energy equations are solved in an iteractive fashion using the standard alternating direction implicit (ADI) technique [16], while the elliptic stream function equation is solved using the method of successive over-relaxation [15]. At each time step the movement of the solid–liquid interface is determined explicitly in accordance with the Stefan condition.

The computations utilize a non-uniform grid spacing in the direction perpendicular to the irregular surfaces. This makes it possible to concentrate a large number of grid points in the critical regions just beneath the free surface (the Marangoni boundary layer) and just adjacent to the solid–liquid boundary. The order of magnitude of the depth of the Marangoni surface layer is given according to

$$\delta_M \propto M^{-1/3} \quad (10)$$

where M is the Marangoni number as defined in Table 3 [17]. In the systems considered, the Marangoni number is of the order of 1×10^4–5×10^4, which implies a dimensionless velocity boundary layer thickness of 0.03–0.05. For each calculation the grid is chosen so as to maintain at least six grid points within the depth of this layer.

RESULTS

Validation of the mathematical model

A number of cases have been computed to test the validity of the coordinate transformation model; these assume a weldpool with a flat free surface so that the results can be compared with previous modelling efforts.

The steady-state calculations of Kou and Sun [4] for the stationary arc welding of aluminum predict a molten pool 1.9 mm deep with a radius of 3 mm, and find maximum velocities of the order of 10 mm s^{-1} for buoyancy forces alone, as compared with 2000 mm s^{-1} for surface tension forces alone.

For the same input parameters (150 A, 15 V, 80% efficiency), the coordinate transformation method predicts a radius and depth of 2.85 and 1.9 mm, respectively, with maximum melt velocities reaching 15 mm s^{-1} for buoyancy-driven flow and 2100 mm s^{-1} for surface tension-driven flow. The penetration profile, flow and thermal fields calculated for surface tension flow, shown in Fig. 2, are in reasonable agreement with those of ref. [4].

As a further test we calculated the transient flow and temperature fields in steel for the same power input (1000 W m^{-2}, spot radius of 0.35 mm), the same weldpool shape and size (radius of 0.7 mm, depth at the axis of 0.3 mm) and the same boundary conditions as reported by Russo *et al.* [17]. The calculation indicates peak surface velocities of 1265 mm s^{-1} after 0.06 ms, in good agreement with the value of 1300 mm s^{-1} reported in ref. [17] at 0.08 ms. The flow patterns and temperature distributions computed using the coordinate transformation model are also in good agreement with their results at 0.08 ms.

Calculations for cathode spot welding of steel

The majority of the results to be presented in this section have been computed using the physical properties of steel given in Table 2 for a Gaussian heat flux distribution appropriate for cathode spot welding ($A=6.135\times10^7$, $B=1\times10^5$). The parameters varied

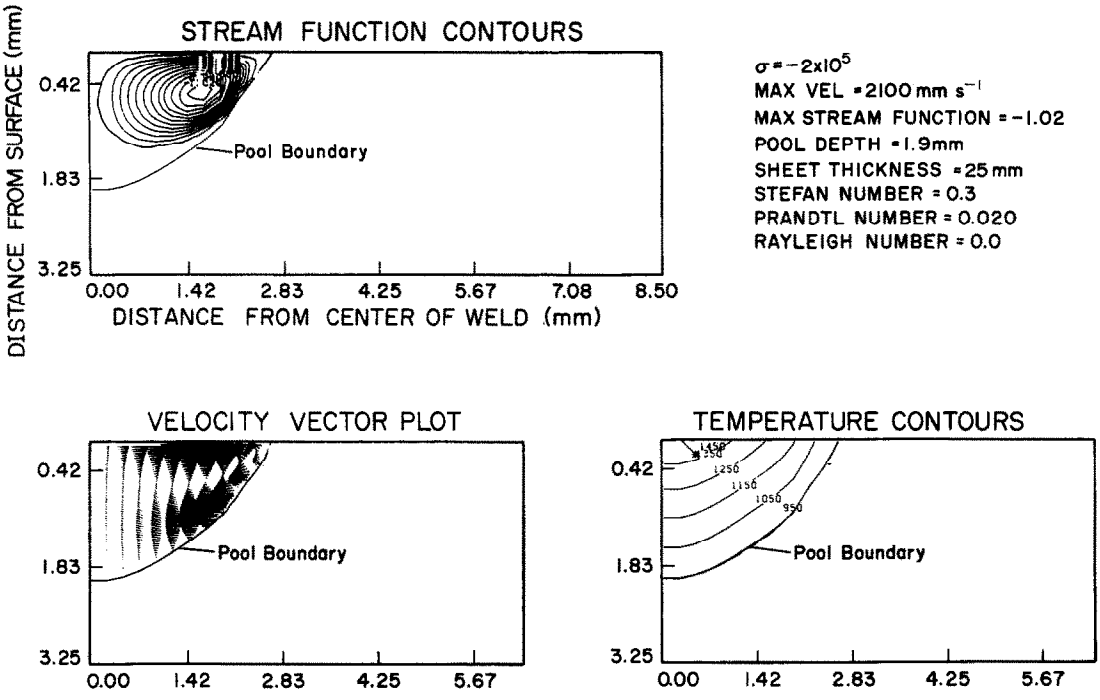

FIG. 2. Computed flow field and temperature distribution in an aluminum weldpool. Flow field shows a clockwise circulation with a maximum value of the stream function of −1.02.

are the central surface depression, the surface tension coefficient (parameter σ) and the buoyancy force. All calculations start with an initial state in which a thin layer of melt of uniform depth (0.5 mm) at the liquidus temperature resides in a 25 mm thick piece of steel at ambient temperature. The width of the computational domain extends 12 mm from the central axis with the basal and outer surfaces of the workpiece held at ambient temperature throughout the calculation.

The reported melt penetration times are based on a dimensionalization scheme in which the length scale is the thickness of the workpiece itself. The melt velocities, on the other hand, are scaled on the basis of the weldpool width and depth at any particular time t.

Figure 3 portrays the effect of the free surface depression on the weld penetration history for pure heat conduction ($\sigma = Ra = 0$). The dashed curves represent the calculated position of the melt–solid interface for a flat free surface. The solid line is the corresponding profile predicted at 5.0 s when the free surface has a maximum central depression extending 1.25 mm beneath the top of the workpiece. The shape of the free surface used in this (and all subsequent) calculations has been based on the double vortex structure described by Lin and Eagar [18, 19].

In reality, the situation is not one of pure heat conduction. The temperature variations within the weldpool produce both buoyancy and surface tension forces, which lead to convective flow of the molten steel. Figure 4 shows weld penetration profiles for a flat and a depressed free surface, calculated assuming that convection in the molten material is governed solely by buoyancy forces. The penetration profiles at 5 s are indistinguishable from the conduction solutions of Fig. 3 for the same welding time. This observation is consistent with the fact that for very low Prandtl number fluids (in typical welding geometries)

Table 2. Physical constants

	Definition	Value for steel	Value for aluminum
ρ	density (kg m^{-3})	7.2×10^{3}	2.4×10^{3}
κ	thermal diffusivity (m^{2}s^{-1})	1×10^{-5}	6×10^{-5}
k	thermal conductivity (W m^{-1}K^{-1})	15/31	100
ΔH	latent heat of fusion (J kg^{-1})	2.47×10^{5}	3.93×10^{5}
ν	kinematic viscosity (m^{2}s^{-1})	7.84×10^{-7}	1.17×10^{-6}
β_T	thermal expansivity (K^{-1})	1×10^{-4}	1×10^{-4}
μ	viscosity (N s m^{-2})	5.6×10^{-3}	2.8×10^{-3}
$\partial\gamma/\partial T$	surface tension coefficient (N m^{-1}K^{-1})	-0.112×10^{-3}	-0.35×10^{-3}
C_p	heat capacity (J kg^{-1}K^{-1})	753	1066

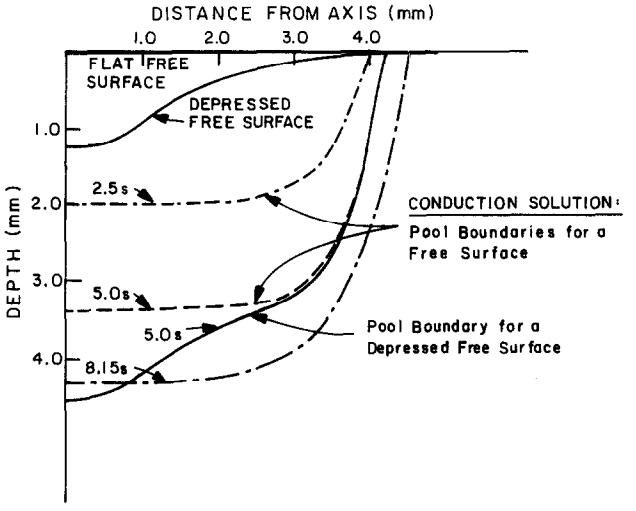

FIG. 3. Calculated weldpool shapes (based on pure conduction) for a pool with a horizontal free surface at 2.5, 5.0 and 8.15 s and a pool with a central axis surface depression of 1.25 mm at 5.0 s (solid line).

subject to buoyancy-driven convection alone, the thermal and velocity fields are essentially decoupled.

The effect of surface tension

The following series of calculations describes combined buoyancy and surface tension-driven convection in weldpools with flat and depressed free boundaries. The magnitude of the surface tension force is represented in the model in terms of σ (Table 3). In the absence of surface active impurities, the surface tension of pure liquid metals decreases with increasing temperature, with the surface tension coefficient for liquid steel being 0.112×10^{-3} N m^{-1} K^{-1}, and that of aluminum, -0.35×10^{-3} N m^{-1} K^{-1} [4, 20–23].

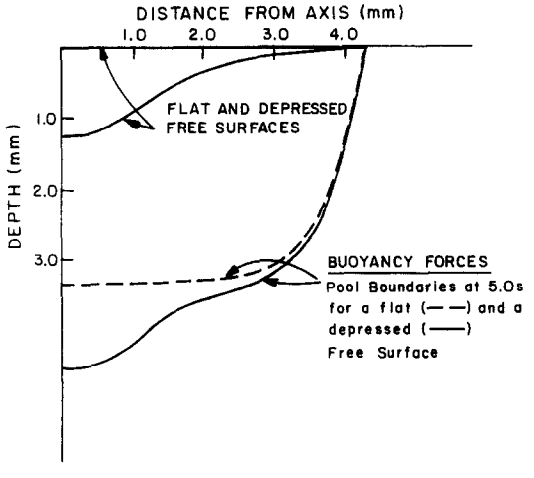

FIG. 4. Weldpool penetration profiles predicted for buoyancy-driven circulation ($Ra = 1 \times 10^4$) for a flat and a depressed free surface at 5.0 s.

The addition of trace amounts of impurities such as S, Se and O, however, can cause $\partial\gamma/\partial T$ and σ to become positive [20–22, 24]. Experimental observations indicate that the presence of these impurities can reverse the direction of fluid motion at the surface of the pool.

The solid and dashed curves of Fig. 5(a) represent melt–solid surfaces in a weld pool with a flat and a depressed free surface, respectively, for $\sigma = -1 \times 10^4$ and $Ra = 1 \times 10^4$. The model predicts a maximum melt depth at the central axis of 3.4 mm at 5.0 s for a pool with a flat free surface. When the free surface is depressed by 1.25 mm at the central axis, the weld penetration depth there is increased by approximately the same amount. At this magnitude of σ, incorporation of surface tension effects produces little change in the penetration profile.

The maximum value of the temperature at the free surface is limited to the vaporization temperature of the liquid. Therefore, as the pool surface is heated, the central portion under the source reaches a constant temperature equal to the maximum allowable surface temperature. Initially this constant temperature region rapidly expands outward from the central axis with the steepest temperature gradients at the free surface occurring just beyond its outer bounds.

The calculated maximum velocities occur at the free surface in the region where the temperature gradients are steepest. The maximum values of the outward surface velocity increase initially during the early stages of melting as the surface is rapidly heated, and reach a peak of 200 mm s^{-1} after approximately 3.5 s. The position of the maximum velocity moves outward with time as the surface temperature profile is established and the magnitude of the velocity decreases gradually, reaching 120 mm s^{-1} after 5 s.

Figure 5(b) compares the shape of the melt–solid

Table 3. Dimensionless parameters

Definition		Value used in calculation steel/aluminum
$Pr = \frac{\nu}{\kappa}$	Prandtl number	0.078/0.02
$Ra = \frac{g\beta_T \Delta T L^3}{\nu\kappa}$	thermal Rayleigh number	1×10^4–5×10^4
$St = \frac{\Delta H}{C_p \Delta T_s}$	Stefan number	0.5/0.3
$K = \frac{k_s}{k_l} = \alpha$	ratio of thermal conductivities of solid and liquid	2.0/1.0
$\sigma = \frac{(\partial\gamma/\partial T)L\Delta T}{\mu\nu}$	surface tension number	0–2×10^5
$M = \frac{(\partial\gamma/\partial T)\partial\Delta T}{\mu\kappa}$	Marangoni number	$\sigma\, Pr$

surface at 3.4 s for a depressed free surface and a positive surface tension coefficient of the same magnitude. The positive surface tension coefficient produces a reverse circulation loop as expected. At this relatively low value of σ the circulation is primarily confined to the outer portion of the pool where the temperature gradients are the steepest. The two weldpool penetration profiles in Fig. 5(b) are quite similar. However, the reverse circulation in the case of a positive σ creates steeper temperature gradients at the base of the pool in the outer region where the circulation is more vigorous. As a result, the pool is slightly deeper there, and narrower at the surface when the surface tension coefficient is positive. This pattern will be even more apparent in calculations at higher (absolute) values of σ.

The calculated maximum surface velocities are about 5% lower with a positive surface tension coefficient than for a negative one. This apparently reflects the fact that buoyancy forces and surface tension forces reinforce one another for negative coefficients, while for positive coefficients the two forces oppose one another. As a check on the validity of the computed results, we can estimate the order of magnitude of the velocity expected for pure surface tension driven flow according to the following:

$$U^3 \sim \frac{\left(\frac{\partial\gamma}{\partial T}\Delta T\right)^2}{\rho\mu L} \tag{11}$$

as derived in ref. [25]. Using the melt depth at the

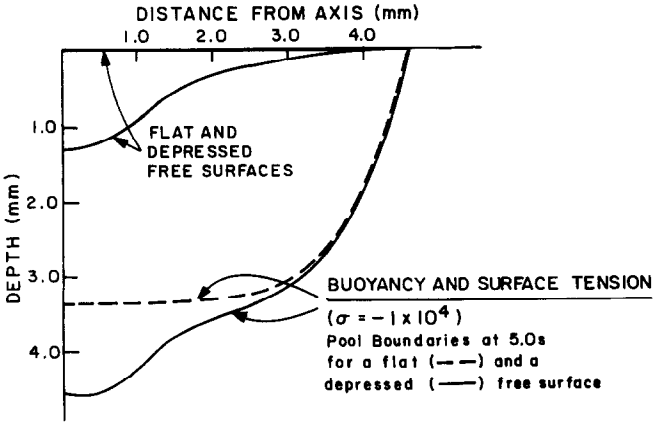

FIG. 5(a). Weldpool penetration profiles predicted for combined surface tension and buoyancy-driven circulation ($Ra = 1 \times 10^4$, $\sigma = -1 \times 10^4$) for a flat and a depressed free surface at 5.0 s.

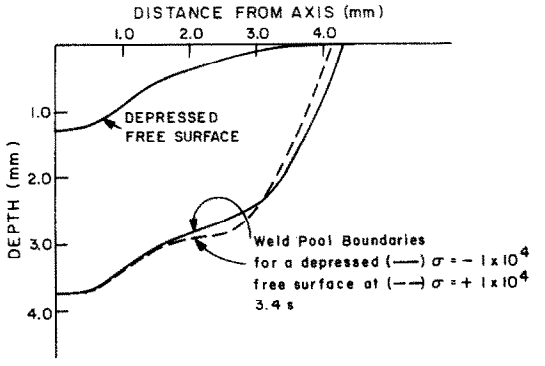

FIG. 5(b). Comparison penetration profiles predicted for positive and negative surface tension coefficients ($Ra = 1 \times 10^4$, $\sigma = \pm 1 \times 10^4$) for a pool with a depressed free surface at 3.4 s.

central axis at any time as the length scale $L(t)$ ($\sigma = 1 \times 10^4$), equation (11) predicts velocities of the order of 150 and 100 mm s^{-1} at 3.46 and 5 s, respectively, in good agreement with those of the numerical simulation.

Figures 6 (flat surface) and 7 (depressed surface) illustrate the penetration profile, flow fields and temperature distribution calculated for $\sigma = -5 \times 10^4$ at 4.3 s. Increasing the magnitude of the surface tension coefficient by a factor of 5 produces little change in the shape of the penetration profile (Fig. 5(a) vs Figs. 6(a) and 7(a)). The maximum velocities, however, are higher, reaching ~ 1000 mm s^{-1} at 2.5 s and decreasing to 500 mm s^{-1} by 4.3 s. Again these calculated velocities are in reasonable agreement with order of magnitude estimates of 600 and 350 mm s^{-1} from equation (11).

As the value of σ is increased, the surface velocity profile is steepened and the boundary layer becomes narrower. The depth of the dimensionless Marangoni velocity layer for $\sigma = 10^5$, for example, is estimated (from equation (10)) to be ~ 0.03. Calculations at high values of σ therefore demand a very fine grid spacing in the vicinity of the free surface. It becomes increasingly difficult to compute flow fields as the value of σ increases, because the stability of the solution and the time required for convergence are directly related to the grid spacing.

Figure 8 compares the penetration profiles for weldpools with flat and depressed free surfaces at 3.12 and 4.25 s ($\sigma = 1 \times 10^5$). As with previous calculations, depression of the free surface by 1.25 mm results in a corresponding increase in melt penetration depth of 1.25 mm at the central axis.

The change in the weldpool shape resulting from an increase in σ from 1×10^4 to 1×10^5 can be seen clearly in Fig. 9 (4.25 s). Melting rates at the central axis for $\sigma = 1 \times 10^5$ are significantly increased over

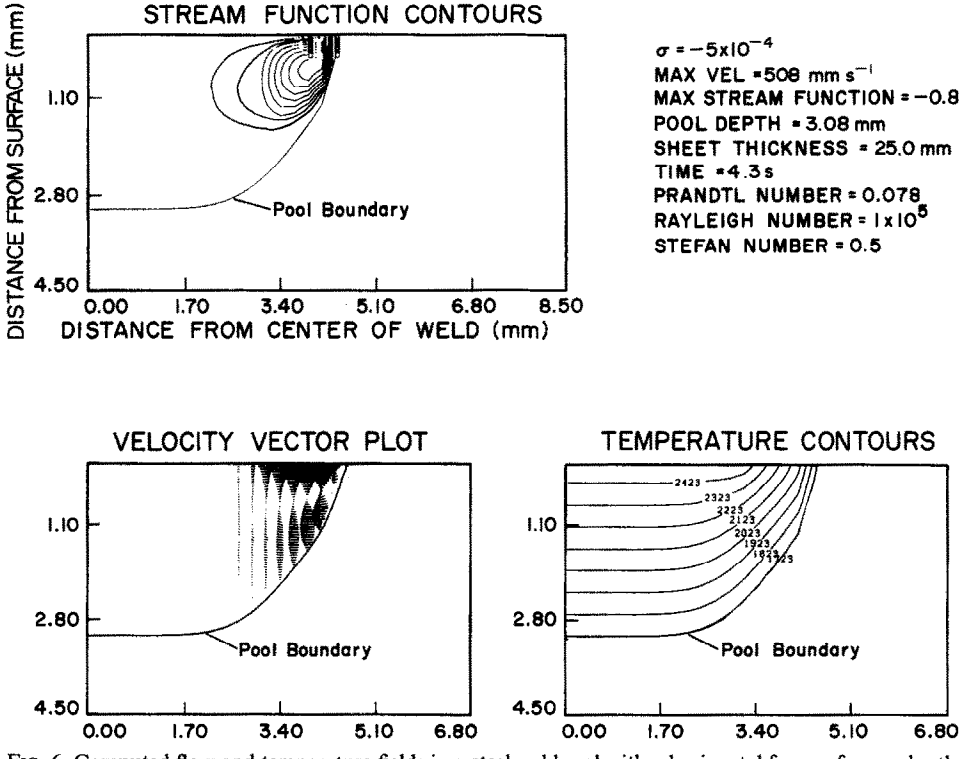

FIG. 6. Computed flow and temperature fields in a steel weldpool with a horizontal free surface under the cathode spot mode of operation at 4.3 s ($Ra = 1 \times 10^4$, $\sigma = -5 \times 10^4$). The flow field shows a clockwise circulation with a maximum value of the stream function of -0.8 and a contour interval of 0.09.

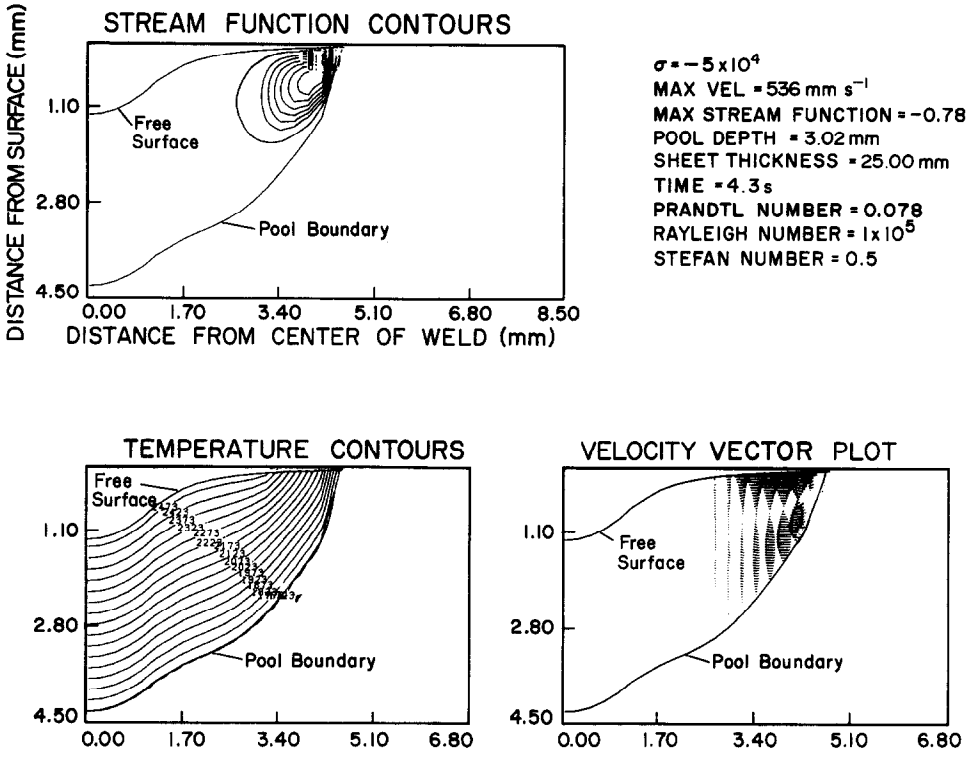

FIG. 7. Computed flow and temperature fields in a steel weldpool with a depressed free surface under the cathode spot mode of operation at 4.3 s ($Ra = 1 \times 10^4$, $\sigma = -5 \times 10^4$). The flow field shows a clockwise circulation with a maximum value of the stream function of -0.78 and a contour interval of 0.09.

those observed for a value of 1×10^4 for similar time intervals (1.5 mm s^{-1} vs 0.5 mm s^{-1} at about 4 s). The width of the weldpool at the surface at any time is approximately the same (as it is primarily governed by the surface heat flux), but beneath the surface the weldpool is significantly narrower and the maximum penetration depth larger at higher (positive) values of σ.

Figure 10 shows the difference in the weldpool shape between melts with positive and negative surface tension coefficients ($\sigma = \pm 1 \times 10^5$). When σ is positive, convective transport of heat is concentrated

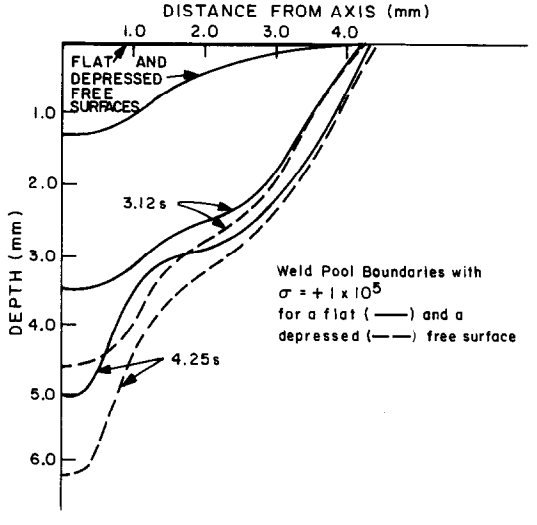

FIG. 8. Comparison of weld penetration profiles predicted for flat vs depressed free surfaces at 3.12 and 4.25 s ($Ra = 5 \times 10^4$, $\sigma = 1 \times 10^5$).

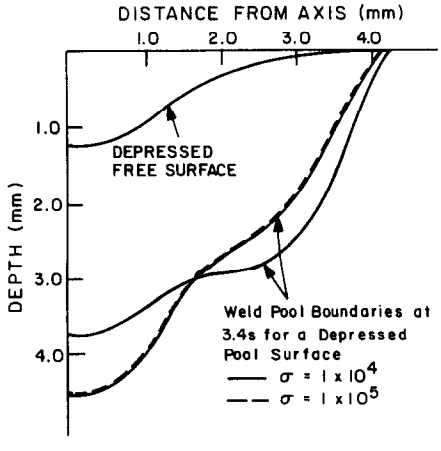

FIG. 9. Comparison of weld penetration profiles predicted in a pool with a depressed free surface for $\sigma = 1 \times 10^4$ vs 1×10^5 at 3.4 s.

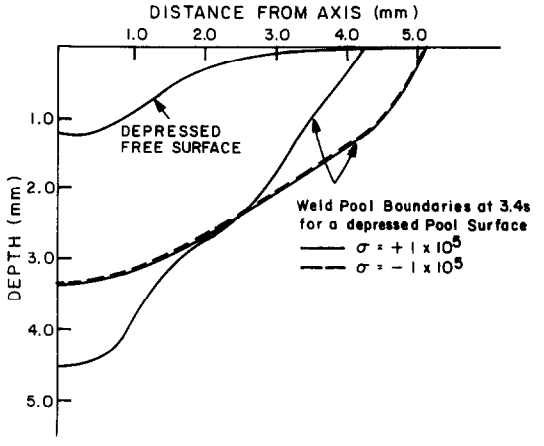

FIG. 10. Comparison of weld penetration profiles predicted in a pool with a depressed free surface for $\sigma = -1 \times 10^4$ vs 1×10^5 at 3.4 s.

downward at the central axis, creating a deep pool (4.7×3.5 mm). When σ is negative, convection is concentrated at the free surface near the pool boundary, creating a wider melt region (5.2 vs 4.3 mm).

Effect of other physical properties

It is also of interest to examine how the physical properties of the material influence the thermal and the velocity fields. Aluminum has a lower Prandtl number than steel (0.02 vs 0.1) and therefore we expect convection to have less of an effect on heat transfer phenomena in aluminum welding applications. However, due to the lower viscosity of aluminum, the calculated σ for a given weldpool dimension will be larger, causing the flow in the pool to be more vigorous.

Figure 11 illustrates the transient melting behavior observed in a thick aluminum sheet (25 mm) supplied with thermal energy from a 150 A, 15 V power source (efficiency, 80%). The input parameters are similar to those used in ref. [4], although the calculation is transient, while theirs are steady state. The calculated melting rates are significantly higher than those predicted for steel welding (see previous calculations), averaging about 5 mm s^{-1} during the first 0.5 s. This is reasonable considering that the Stefan number is smaller, the thermal conductivity of molten aluminum is approximately five times as large, and the ratio of liquid to solid thermal conductivities is also higher for aluminum. Furthermore, the aluminum calculations

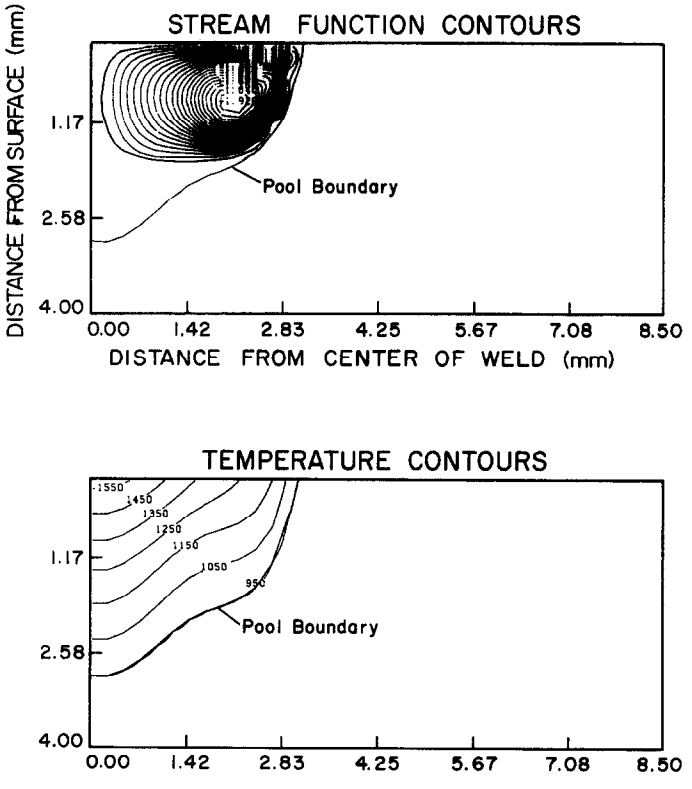

$\sigma = -2 \times 10^5$
MAX VEL = 2432 mm s^{-1}
MAX STREAM FUNCTION = -1.92
POOL DEPTH = 2.93 mm
SHEET THICKNESS = 25.00 mm
TIME = 1.0 s
PRANDTL NUMBER = 0.020
RAYLEIGH NUMBER = 0.0
STEFAN NUMBER = 0.3

FIG. 11. Computed flow and thermal fields in an aluminum weldpool with a flat surface for a value of $\sigma = 2 \times 10^5$ after 1.0 s. The flow field shows a clockwise circulation with a maximum value of the stream function of -1.92 and a contour interval of 0.08.

use a slightly more intense power source than those reported for steel.

It is seen that the circulation is confined to the upper two-thirds of the pool. The shape of the weldpool results from the combination of vertical conduction, which is strongest at the central axis, and convective heat transport which has a significant horizontal component and is concentrated in the outer portions of the pool. This explains the distinctive double-well penetration profile frequently found in practice.

The calculated maximum velocities in the aluminum weldpool are in general agreement with those estimated from equation (11) (1500 mm s^{-1}), and those reported in ref. [4] of 2000 mm s^{-1} for their steady-state calculations.

These results are compatible with the findings of Chan *et al.* [23], who found that the decrease in *Pr* from steel to aluminum increases the maximum surface velocity by a factor of approximately 5; furthermore, for otherwise identical conditions the depth of melt penetration in aluminum is 3–4 times larger than for steel.

Comparison with experimental results on stainless steel

As a final step, we use the coordinate transformation method to model the GTA spot welding experiments described by Giedt *et al.* [26] on 304 and 303S stainless steel, which involved heating 5 mm thick disks of steel using a 200 A, 17 V (40% efficiency) power source with an assumed radius of 5.9 mm [26]. The specimens were heated for 3.5 s; then the heat source was disconnected, and the surface temperatures measured starting at 3.7 s. For the 304 stainless steel, which has a negative surface tension coefficient, the final measured pool dimensions were 2.3 mm (depth at axis) by 4.5 mm (radius), as compared to 4.06 mm (depth) by 4.0 mm (radius) for 303S stainless steel with a positive surface tension coefficient.

Using the experimental conditions described in ref. [26], the coordinate transformation was used to analyze the melting period (0–3.5 s). The weldpool penetration profiles and flow patterns calculated after 3.2 s are shown in Fig. 12. The predicted weldpool dimensions are in general agreement with those reported in ref. [26]. The outward surface flow which arises when σ is negative creates a shallow pool with a predicted depth at axis of 2.3 mm and a radius of 4.6 mm, while flow is inward with a positive surface tension coefficient creating a pool 4.2 mm deep by 4.0 mm wide.

There is, however, a difference between the calculated time for heating and the actual time reported in the experiments (<0.5 s). This most likely reflects the fact that radiation and surface convection effects have not been incorporated into the mathematical model. As a result, the predicted surface temperatures exceed the actual surface temperatures, and the predicted melting rates are slightly higher than those observed in the experiments.

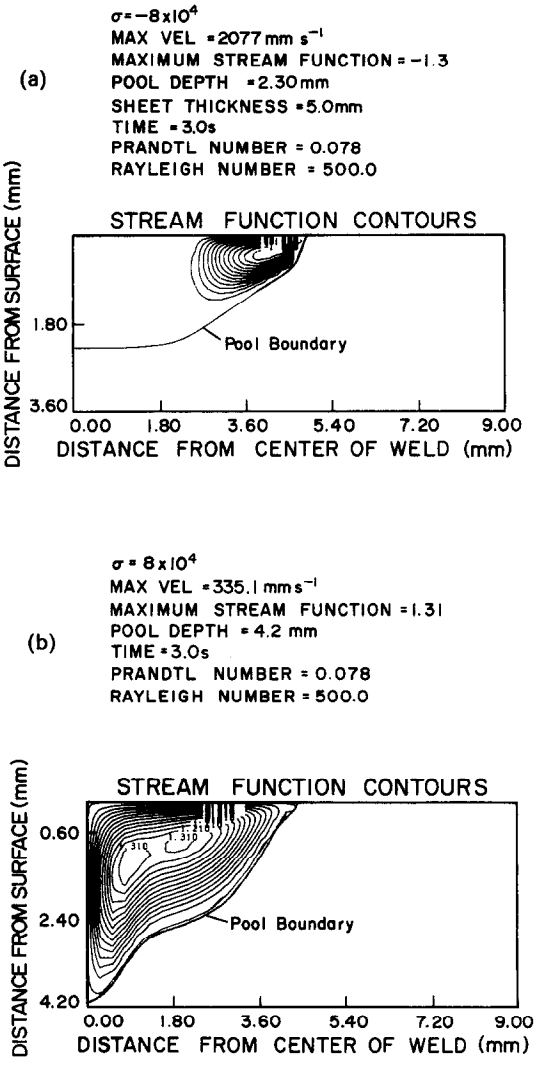

FIG. 12. Comparison of computed flow and thermal fields for 304S, equation (12a), and 303, equation (12b), stainless steel weldpools with a flat surface after 3.0 s. The flow field for 304S shows a clockwise circulation with a maximum value of the stream function of -1.3 and a contour interval of 0.1, while that for 303 shows a counterclockwise circulation.

CONCLUSIONS

We have shown that the two-dimensional coordinate transformation is an effective method for investigating transport phenomena in weldpools when either a deformed free surface and/or a moving solid–liquid interface is present. This approach not only simplifies computation of the motion of the phase boundary, but also provides a very accurate means for prescribing the conditions at the free surface and calculating the surface tension forces.

The calculations confirm previous findings [3, 4, 25, 27] concerning the relative importance of buoyancy and surface tension forces in driving convection, and predict velocities of the order of 10–50 mm s^{-1} for

buoyancy forces alone, and anywhere from 100 to 3000 mm s^{-1} for combined surface tension and buoyancy-driven flow. For otherwise identical input conditions, the depression of the free surface causes a change in the calculated maximum velocity at the free surface of less than 10%. However, the presence of the central depression in the free surface has a very significant effect on the shape of the weld penetration profile. This is true regardless of the magnitude and/or the sign of the surface tension coefficient. In fact, for the range of σ examined thus far, the calculations show that the increase in the depth of the penetration profile over that predicted for a horizontal free surface is approximately equal to the extent to which the free surface is depressed.

At low values of σ, convection within the molten region has little influence on the rate of melt penetration. Once σ exceeds $\sim 5 \times 10^4$, however, convective motion in the weldpool begins to have a significant effect on the thermal field and the melting rates. This is an important observation, as it provides a means for determining the welding conditions under which convection can, or cannot, be expected to influence the characteristics of the weld. It will be particularly useful when more accurate experimental data concerning the variation of surface tension with impurity content become available. For practical purposes, differences in σ can be expected between various materials, for different power sources, for weldpools of different dimensions, and for materials with different types of surface active impurities.

At higher values of σ, the shape of the weld penetration profile reflects the combined effect of the free surface depression and convective heat transfer within the pool. When the surface tension coefficient is large and negative, fluid at the free surface moves outward, transporting heat from the central axis toward the edge of the pool. The result is the formation of a shallower, broader pool than is predicted at lower values of σ. Alternatively, when the surface tension coefficient is positive, surface flow is radially inward and the penetration depths at the axis are much greater.

Although these findings are not entirely new [3, 25], the calculated shapes of the weldpools are thought to be rather more precise and differ somewhat from those reported earlier [3, 23, 25]. Calculations based on a positive surface tension coefficient predict a weldpool characterized by a very deep narrow root, which widens close to the surface. When the surface tension coefficient is negative, the circulation becomes progressively restricted to the outer edges of the pool with time. As a result, melt rates are highest at the central axis, decrease outward, and then for high-σ melts, may actually increase slightly at some distance between the axis and the pool edge. Finally, a point which in retrospect appears obvious, but is of great practical importance, is that for all cases examined, depressing the free surface increases the weld penetration depth by a corresponding amount.

Acknowledgements—The authors are grateful to the National Science Foundation and the Materials Processing Center of MIT for partial support of this project under Grant #82-10849-CPE, and to the National Aeronautics and Space Administration for partial support under Grant #NSG-7645, administered by the Materials Processing Center of MIT.

REFERENCES

1. O. H. Nestor, Heat intensity and current distribution at the anode of high current inert gas arcs, *J. Appl. Phys.* **33,** 1638–1648 (1962).
2. C. B. Shaw, Jr., Effect of orifice geometry in plasma arc welding of Ti–6Al–4V, *Welding J.* **59,** 121s–125s (1980).
3. G. M. Oreper, J. Szekely and T. W. Eagar, The role of transient convection in the melting and solidification in arc weldpools, *Metall. Trans.* **17B,** 735–751 (1986).
4. S. Kou and D. K. Sun, Fluid flow and weld penetration in stationary arc welds, *Metall. Trans.* **16A,** 203–213 (1985).
5. G. M. Oreper, T. W. Eagar and J. Szekely, Heat and fluid flow phenomena in weldpools, *J. Fluid Mech.* **147,** 53–79 (1984).
6. H. G. Landau, Heat conduction in a melting solid, *Q. Appl. Math.* **8,** 81–94 (1950).
7. N. Ramachandran and J. P. Gupta, Two-dimensional solidification with natural convection in the melt and convective and radiative boundary conditions, *Numer. Heat Transfer* **4,** 469–484 (1981).
8. J. L. Duda, M. F. Malone, R. H. Notter and J. S. Vrentas, Analysis of two-dimensional diffusion controlled moving boundary problems, *Int. J. Heat Mass Transfer* **18,** 901–910 (1975).
9. A. Gadgil and D. Gobin, Analysis of two-dimensional melting in rectangular enclosures in the presence of convection, *Trans. ASME* **106,** 20–26 (1984).
10. C. J. Ho and R. Viskanta, Heat transfer during melting from an isothermal vertical wall, *ASME J. Heat Transfer* **106,** 12–19 (1984).
11. C. F. Hsu, E. M. Sparrow and S. V. Patankar, Numerical solution of moving boundary problems by boundary immobilization and a control-volume-based finite difference scheme, *Int. J. Heat Mass Transfer* **24,** 1335–1343 (1981).
12. T. Saitoh, Numerical method for multidimensional freezing problems in arbitrary domains, *ASME J. Heat Transfer* **100**(2), 294–299 (1978).
13. E. M. Sparrow, S. V. Patankar and S. Ramadhyani, Analysis of melting in the presence of natural convection in the melt region, *Trans. ASME* **99,** 520–526 (1977).
14. M. E. Thompson, Double-diffusive phenomena in horizontally-solidified binary liquids, Ph.D. Thesis, Department of Materials Science and Engineering, Massachusetts Institute of Technology (1986).
15. P. J. Roache, *Computational Fluid Dynamics*. Hermosa, Albuquerque, New Mexico (1972).
16. D. W. Peaceman and H. H. Rachford, Jr., The numerical solution of parabolic and elliptic differential equations, *J. Soc. Ind. Appl. Math.* **3**(1), 28–41 (1955).
17. A. J. Russo, R. L. Akau and J. L. Jellison, Thermocapillary flow in a pulsed laser weldpool, *Welding J.* (1989), in press.
18. M. L. Lin and T. W. Eagar, Influence of surface depression and convection on arc weldpool geometry. In *Transport Phenomena in Materials Processing*, ASME-PED Vol. 10, pp. 63–69 (1983).
19. M. L. Lin and T. W. Eagar, Influence of arc pressure in GTA welding, *Weldpool J.* **64,** 163 (1985).
20. C. R. Heiple and P. Burgardt, Effects of SO_2 shielding gas additions on GTA weld shape, *Welding J.* **64,** 160–162 (1985).
21. C. R. Heiple and J. R. Roper, Mechanism for minor

element effects on GTA fusion zone geometry, *Welding J.* **61**, 97–102 (1982).
22. C. R. Heiple and J. R. Roper, Effects of minor elements on GTAW fusion zone shape. In *Trends in Welding Research in the U.S.* (Edited by S. A. David), pp. 489–522. American Society for Metals, Metals Park, Ohio (1981).
23. C. Chan, J. Mazumder and M. J. Chen, A two-dimensional transient model for convection in a laser melted pool, *Metall. Trans.* **15A**, 2175–2184 (1984).
24. B. J. Keene, K. C. Mills, J. W. Bryant and E. D. Hondros, Effects of interaction between surface active elements on the surface tension of iron, *Can. Metall. Q.* **21**, 393–403 (1982).
25. G. M. Oreper and J. Szekely, Heat and fluid flow phenomena in weldpools, *J. Fluid Mech.* **147**, 53–79 (1984).
26. W. H. Giedt, X. C. Wei and S. R. Wei, Effect of surface convection on stationary GTA weld zone temperatures, *Welding J.* **63**, 376–383 (1984).
27. G. M. Oreper, T. W. Eagar and J. Szekely, Convection in arc weldpools, *Welding J.* **62**, 307–312 (1983).

COMPORTEMENT VARIABLE DE BAINS DE SOUDURE AVEC UNE SURFACE LIBRE DEFORMEE

Résumé—Le transfert thermique, l'écoulement et le changement de phase en régime variable dans un bain du fusion, avec une surface libre déformée, sont modélisés en utilisant une transformation bidimensionnelle de coordonnées. L'approche théorique rend possible la modélisation précise des écoulements à grand nombre de Marangoni, même quand la surface libre n'est pas horizontale. La méthode est utilisée pour examiner le rôle de la déformation de la surface et des forces interfaciales dans la pénétration de la soudure pendant le soudage cathodique de l'acier et de l'aluminium. Les champs d'écoulement calculés, les distributions de température et les formes des bains liquides sont cohérents avec les résultats expérimentaux et ils sont en accord raisonnable avec des modèles antérieurement publiés.

DAS TRANSIENTE VERHALTEN EINES SCHWEISSBADES MIT EINER DEFORMIERTEN FREIEN OBERFLÄCHE

Zusammenfassung—Mit Hilfe einer zweidimensionalen Koordinatentransformation werden Wärmeübergang, Strömung, Phasenwechsel in einem Schweißbad mit einer deformierten freien Oberfläche modelliert. Der theoretische Ansatz ermöglicht eine genaue Nachbildung von Strömungen mit hoher Marangoni-Zahl, sogar bei nicht-horizontaler freier Oberfläche. Die Methode wird benutzt, um den Einfluß der Oberflächendeformation und der Oberflächenspannung bei der Regelung der Schweißtiefe beim Kathoden-Punktschweißen von Stahl und Aluminium zu untersuchen. Die berechneten Strömungsfelder, Temperaturverteilungen und Schmelzformen stimmen sowohl mit experimentellen Ergebnissen als auch mit anderen veröffentlichten Modellen überein.

ПЕРЕХОДНЫЙ РЕЖИМ В СВАРОЧНЫХ ВАННАХ С ДЕФОРМИРОВАННОЙ ПОВЕРХНОСТЬЮ

Аннотация—С помощью двумерных преобразований координат моделируются неустановившийся теплоперенос, течение жидкости и фазовый переход в сварочной ванне с деформированной свободной поверхностью. Теоретический подход позволяет предложить точную модель течения при высоких числах Марангони даже в случае негоризонтальной свободной поверхности. Метод использован для изучения роли деформации поверхности и сил поверхностного натяжения в процессе регулирования глубины проплавления при катодной точечной сварке стали и алюминия. Рассчитанные поля течения, распределения температур и формы сварочных ванн соответствуют экспериментальным данным и хорошо согласуются с ранее предложенными в литературе моделями.